Chapter 6

Sinuous Antenna Coupled TES bolometers

6.1 Introduction

Results from Chapter 5 suggest that the sinuous antenna is a promising candidate for coupling to TES-bolometers in CMB detectors. In this chapter, we describe the design, fabrication and testing of prototype pixels that are the simplest possible integration of the sinuous with the proven detector technology from Polarbear. Measurements of these devices demonstrate successful coupling of the sinuous to bolometers with high optical throughput and desirable beam characteristics.

The chapter begins with a discussion of the microwave electronics used to couple the sinuous antenna to our bolometers. We also describe our optical test cryostat used for all measurements in this thesis as well as an interferometer used to verify the filters' spectra. Finally, we show the results of several optical measurements and compare them against simulations.

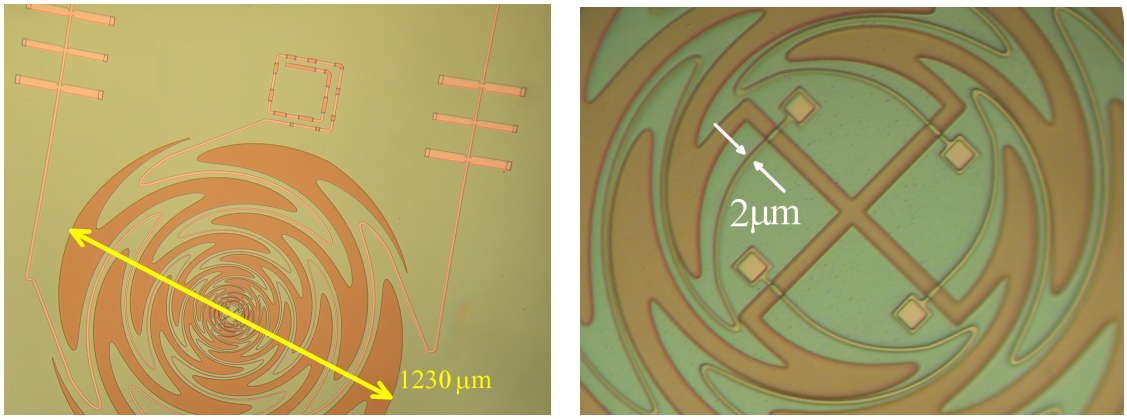

(a) Prototype Pixel (b) Zoom of Antenna Center

Figure 6.1. (a) Photograph of a prototype sinuous antenna; one polarization is terminated, the other passes through identical bandpass filters before the bolometer (not pictured). (b) Zoom of the antenna interior. The 1 μm microstrip alignment error in this picture was not present on the tested devices.

6.2 Microwave design considerations for the Prototype Chips

Figure 6.1 is a photograph of a prototype pixel. To optically characterize the antenna beams in different spectral regions, we fabricated five different devices with identical antennas but different bolometers and filters tuned to receive 30% passbands centered at 86GHz, 110GHz, 150GHz, 180GHz, and 230GHz . After the antenna, the power:

1. couples to microstrip transmission lines integrated onto antenna arms
2. passes through band defining microstrip filters
3. thermally deposits power at the bolometer on a lumped resistive load (not shown)

In the following subsections, we describe each of these stages.

6.2.1 Microstrip transmission lines

Microstrip transmission lines have a conducting metallic strip of width W separated from a ground plane by an insulating dielectric material of thickness h. Currents that travel in the upper conductor are mirrored by return currents in the ground plane. The currents generate electric fields between the two conductors and magnetic fields that circulate the

upper conductor (See figure 6.2). Microstrip transmission lines are popular for lithographed circuits because they are simple to fabricate in thin films.

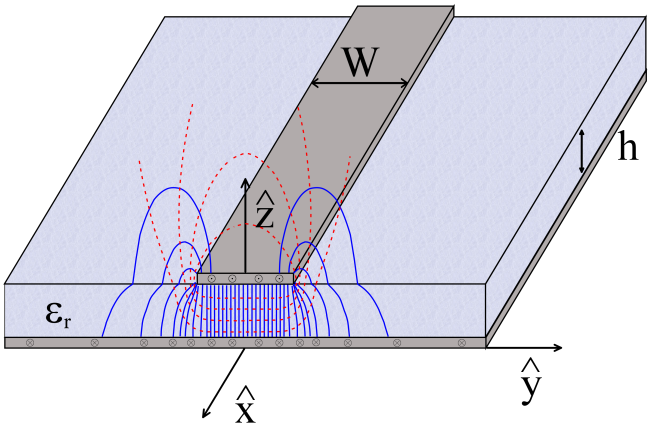

(a) Microstrip fields

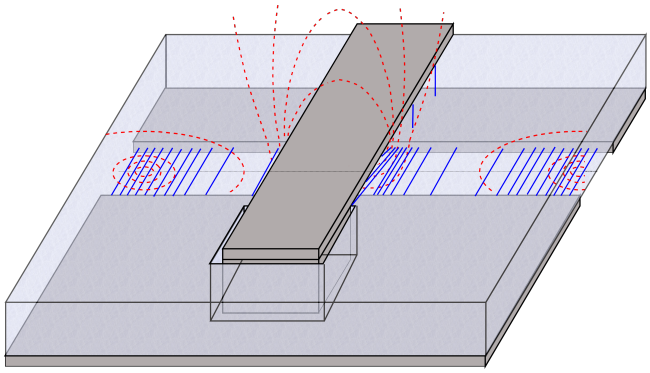

(b) Slot-transition fields

Figure 6.2. Drawing of Microstrip (a). Nb is gray, SiO_2 is light blue. Electric fields are in solid blue, while magnetic fields are dashed red. They kink at the free-space/dielectric interface. At a slot (b), the E-fields "fold" across the slot leaving the magnetic fields normal. Power propagates down the slot away from the microstrip.

We couple slot antennas (such as our sinuous) to microstrips by carving slots into the ground plane, crossing the upper conductor over the slots, and finally shorting to ground on the opposite side. This feed geometry forces the electric fields from the transmission lines onto the antenna's plane, oriented across the slots. The magnetic fields are normal to the slots, so the electric currents a the slot edge are equivalent to magnetic currents that propagate down the slot's interior (*Gupta et al.* [1996]). cross the slots. The magnetic fields

are normal to the slots, so the electric currents a the slot edge are equivalent to magnetic currents that propagate down the slot's interior (*Gupta et al.* [1996]).

Fabrication

In order of deposition, the microstrips are composed of:

1. 3000 Å sputtered Niobium (Nb) ground-plane. (nominally, $\lambda \sim 1000$Å)
2. 5000 Å PECVD SiO_2 dielectric layer ($\epsilon_r = 3.9$)
3. 6000 Å sputtered Nb upper-conductor.

PECVD stands for Plasma Enhanced Chemical Vapor Deposition and is a process that forms the oxide entirely from reacting gases N_2O and SiH_4 (*Chang* [2010b]). The Nb sputtering process also uses an Argon plasma to knock Nb atoms from a target and deposit them on our wafers. We deposited these layers between the LSN and Al-Ti layers described in the bolometer fabrication section of Chapter 3. To ensure a superconducting connection between Nb layers at via shorts, as well as between Nb and Al-Ti at the bolometers terminations, we sputter etch with an Ar plasma to remove native Nb-oxide prior to those metallic depositions.

We chose the SiO_2 thickness of 5000Å to provide relatively high impedance lines, but not so thick that it would cause mechanical issues through internal stress or electrical issues associated with step coverage through the vias between upper and lower Nb films. We chose the Nb ground thickness of 3000 Å to exceed the superconducting magnetic field penetration depth of 1000 Å (*Kerr* [1999]) and the upper Nb thickness of 6000 Å to ensure step coverage in the vias.

We defined all of our features with standard optical photolithography and etched the films with a CF_4 plasma (*Hamilton* [2010]). We mixed the CF_4 with trace amounts of O_2 to wear away the photoresist during etching, providing more gradual side-walls that further helps step-coverage. In principle, the lithography can provide sub-micron resolution (*Meng* [2010]), but the O_2 over-etches the features, rendering it impractical to make features finner

than 1 μm in the 6000 Å thick Nb. We can improve the etching resolution with thinner films of Nb in the upper-layer, but not without compromising step coverage in the vias. Our group is currently exploring new fabrication techniques to address this constraint, but all devices described in this thesis were limited in resolution to 1 μm. Other research groups have achieved sub-micron widths of Niobium lines with comparable thickness by using liftoff lithography and this may be a possible solution for our process in the future.

Fringing fields

Despite being relatively easy to make, microstrip is not true TEM transmission line because of the kink in the fringing fields between fee-space and dielectric (see Figure 6.2). At that interface, the Magnetic fields **H** are continuous because μ_r=1. The change Δ in normal field H_z across the interface is related to the tangential electric fields (E_x, E_y) there through Faraday's law:

$$\begin{aligned} 0 &= \Delta\left[\mathbf{H}_z\right] \\ &= \Delta\left[(\nabla \times \mathbf{E})_z\right] \\ &= \Delta\left[\frac{\partial E_x}{\partial y}\right] - \Delta\left[\frac{\partial E_y}{\partial x}\right] \end{aligned}$$

Because ϵ_r changes as the fields cross this surface, E_y is also discontinuous there. To keep **H** continuous, the fringing longitudinal component E_x cannot vanish. A similar argument shows that **H** also has longitudinal components. Since these components are small compared to the fields between the conductors, microstrips are "quasi-TEM" transmission lines and are only slightly dispersive (*Gupta et al.* [1996]). But we must account for these fringed fields when calculating microstrip impedance.

Kinetic Inductance

Superconducting effects enter into this calculation. The circuit model for an ideal *lossless* transmission line has series inductance L and shunt capacitance C per unit length, providing

an impedance $Z = \sqrt{L/C}$ and wave speed $v = 1/\sqrt{LC}$. A *lossy* normal transmission line has shunt resistance per length corresponding to dielectric losses and series resistance per length from Ohmic losses in the metal (See figure 6.3(a), *Pozar* [2004]). However, superconductors are *not* just ideal, lossless metals; the ohmic series resistance R_Ω present from normal metals becomes an extra source of inductance L_K (See figure 6.3(b)).

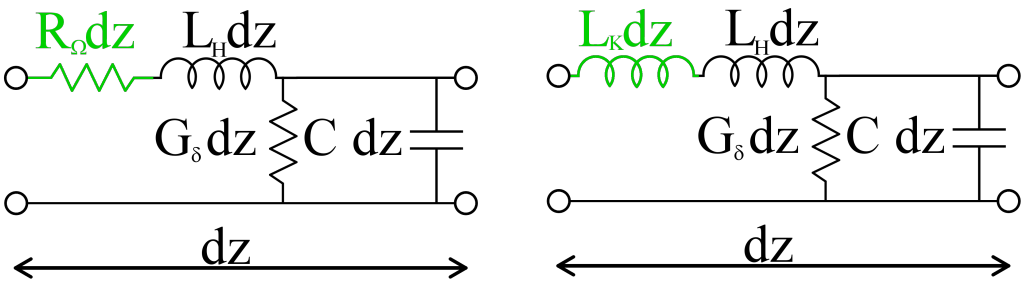

(a) Normal Transmission line (b) Superconducting Transmission line

Figure 6.3. Circuit Models for transmission line section of length dz. When cooled below the conductor's superconducting transition, the ohmic series resistance becomes inductive.

In the Drude-model of conduction, electrons in a metal experience forces from applied fields E and well as a frictional forces cause by collisions every time-constant τ (*Kittel* [2004]).

$$m\frac{d\langle v\rangle}{dt} = -eE - m\frac{\langle v\rangle}{\tau}$$

The conductivity is proportional to the velocity with which the electrons travel through the metal. For a superconductor with no collisions, $\tau \to \infty$, so currents with frequency ω will have a conductivity:

$$\sigma = -j\frac{ne^2}{m\omega} \tag{6.1}$$

where n is the number-density of current-carrying particles (*Van Duzer* [1998]). In contrast to the real σ for a normal metal, this causes the current to lag behind the voltage

just like an inductor. For a conductor of cross sectional area A, the inductance per unit length of this metal is

$$L_K = m/(ne^2A)$$

and the associated energy per volume is

$$\frac{L_K I^2/2}{A} = n\frac{1}{2}m\langle v\rangle^2$$

This phenomenon is termed kinetic inductance because it's created by the large kinetic energy that current carrying particles acquire in superconductors. It is suppressed in normal metals by the low scattering times τ (*Van Duzer* [1998]).

Electromagnetic waves are screened from the interior of superconductors beyond a penetration depth $\lambda = \sqrt{m/\mu_o ne^2}$. So the kinetic inductance is only relevant in the volume on the outer surface with cross-sectional area $A = W\lambda$, providing an inductance per unit length of:

$$L_K = \mu_o\lambda/W \tag{6.2}$$

(*Kerr* [1999]). Ignoring fringing fields, the magnetic inductance is $L_H/ = \mu_o h/W$. For our transmission lines with oxide films 5× thicker than λ, L_K is about 20% of L_H. So this effect makes a substantial contribution of $\sim$ 10% to the impedance and wavespeed. It is convenient to express the inductance in units per square of material, so L_K=$\mu_o\lambda\approx 0.13pH/\square$.

The shunt conductance to ground G_Ω in Figure 6.3 represents losses in the SiO_2 dielectric medium. We have previously measured the loss tangent of our SiO_2 to be $\tan(\delta)$=0.005, which corresponds to 4% loss per millimeter at a frequency of 150GHz.

Yassin and Witherton developed a detailed model for superconducting microstrips with fringed fields (*Yassin and Withington* [1996]). However, it is cumbersome to integrate this model with full-wave EM simulators like Sonnet EM. Sonnet uses a very similar algorithm to ADS-momentum, modeling the non-perfect conducting metallic surfaces with a surface

impedance to allow for small tangential electric fields. Sonnet is the best choice for broad-band superconducting applications because it allows the user to choose to input a surface inductance (*Kerr* [1999]). We have found good agreement of microstrip impedances and wave speeds between the analytic model and ADS with a surface inductance.

Dolph-Chebyshev Transformer

The average impedance of the sinuous antenna is Z_{ant}=105Ω, but we normalized our microstrip circuits to an impedance of Z_{line}=10Ω which corresponds to 10 μm wide lines. Such an abrupt change in impedance would reflect away over 80% of the power. Instead, we gradually change the impedance with a tapered line width. We taper our impedance with the a Dolf-Chebyshev transformer:

$$Z(x) = Z_{ant} \exp\left\{\frac{1}{2}\ln\left(\frac{Z_{low}}{Z_{high}}\right)\left[\sin\left(\pi\left(\frac{x}{L}-\frac{1}{2}\right)\right)+1\right]\right\} \tag{6.3}$$

along the backs of the antenna arms over a length L=4.5mm (*McGinnis and Beyer* [1988]). In practice, we cannot fabricate lines with impedance any higher than ∼60Ω without a major change to our fabrication process (*Meng* [2010]), but this mismatch only reflects 8% of the power. We leave fabrication of 100 Ω lines to future efforts. As described below, this mismatch creates a standing wave that we use to constrain the antenna impedance.

6.2.2 Quarter-wavelength shorted stub filters

Terrestrial observations require bands that are wide enough to received high integrated power, but also edges that are steep enough to reject atmospheric lines. Steeper edges can provide higher throughput, but they require more resonant poles which have enhanced loss over non-resonant microstrip features. A good compromise is a 3-pole filter. For more detail on this optimization, we refer the reader to Kam Arnold's thesis (*Arnold* [2008]).

Figure 6.4 shows a generic 3-pol filter. The values of the inductors and capacitors can

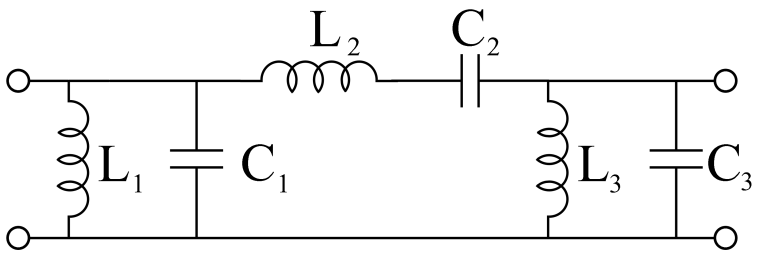

Figure 6.4. Generic 3-pole bandpass filter. At resonance, the series resonator conduct and parallel resonators to ground open.

be chosen to tailor the filter's bandwidth and ripple (*Matthaei et al.* [1980]). The parallel LC resonators on the left and right have an impedance of

$$\begin{aligned} Z_{parallel} &= \left(j\omega L + \frac{1}{j\omega C} \right)^{-1} \\ &\approx -\frac{j}{2\omega_o C} \frac{\omega_o}{\delta\omega} \end{aligned} \tag{6.4}$$

where the last line is an expansion for small differences in frequency $\delta\omega$ from the resonant frequency ω_o. Likewise, the series LC filter in the center has impedance:

$$\begin{aligned} Z_{series} &= j\omega L + \frac{1}{j\omega C} \\ &\approx j2\omega_o L \frac{\delta\omega}{\omega_o} \end{aligned} \tag{6.5}$$

It is challenging to realize these lumped electrical components in millimeters wave circuits because their properties will depend on fine micron-scale dimensional details. Alternatively, we can make equivalent circuits with distributed resonators on transmission lines (*Myers et al.* [2005]). Waves on a transmission line with impedance Z_o will partially reflect off a termination Z_L and interfere with the incoming waves to form a standing wave. At a distance ℓ from the load on a *lossless* line, the ratio of voltage to current in the standing waves creates a transformed impedance of

$$Z_{in} = Z_o \frac{Z_L + jZ_o \tan(2\pi\ell/\lambda)}{Z_o + jZ_L \tan(2\pi\ell/\lambda)} \tag{6.6}$$

(*Pozar* [2004]). If the line is $\ell = \lambda_o/4$ long with impedance Z_1 and the loading impedance is a short to ground ($Z_L = 0$), the input impedance expanded around the resonant frequency ω_o is:

$$\begin{aligned} Z_{in} &= jZ_1 \tan\left(\frac{\pi}{2}\frac{\omega_o + \delta\omega}{\omega_o}\right) \\ &= jZ_1 \cot\left(\frac{\pi}{2}\frac{\delta\omega}{\omega_o}\right) \\ &\approx -jZ_1\frac{2}{\pi}\frac{\omega_o}{\delta\omega} \end{aligned} \tag{6.7}$$

This is exactly the same form as the impedance of the parallel LC resonator. If we choose the impedance Z_1 to match the pre-factor in Equation 6.4, a shorted $\lambda/4$ transmission line will behave identically to the LC filter for frequencies near ω_o.

When we view a general load impedance Z_L through a $\lambda/4$ long line of impedance Z_{inv}, Equation 6.6 reduces to

$$Z_{in} = \frac{Z_{inv}^2}{Z_L} \tag{6.8}$$

The $\lambda/4$ line with impedance Z_{inv} is an inverter that inverts the load impedance (*Pozar* [2004]). If the load is the shorted $\lambda/4$ resonator described above (but with another impedance Z_2), then it's impedance will look like:

$$Z_{in} = j\frac{\pi}{2}\frac{Z_{inv}^2}{Z_2}\frac{\delta\omega}{\omega_o} \tag{6.9}$$

which has the same form as the series resonator. As before, this will behave identically to a series resonator with the proper choice of Z_{inv} and Z_2 .

We can replace the three-pole filter in Figure 6.4 with the filter shown in 6.5 (*Matthaei et al.* [1980]). It has three pairs of $\lambda/4$ shorted stubs separated by two $\lambda/4$ inverters. Once we have chosen a pass-band center frequency ω_o, we can control the input impedance, band ripple and width with the impedances of (1) the outer stubs, (2) the inner stub, and (3) the inverter. In practice, it is easiest to do this numerically with an optimizer algorithm and

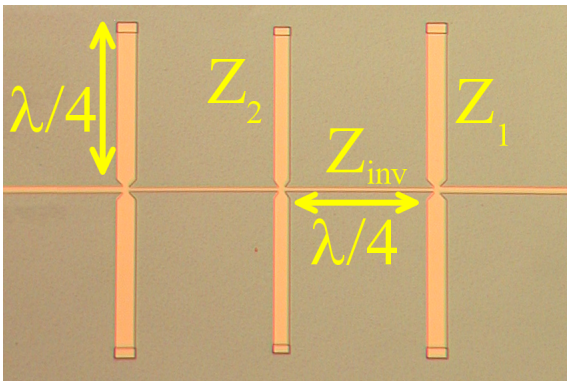

Figure 6.5. Stub filter with shorts through the square vias at the ends.

we chose the impedances, widths and lengths shown in the Chart 6.5. We build pairs of parallel stubs instead of single stubs to avoid microstrips so wide that they might be driven in non-fundamental modes.

The transmission-line filter only approximates the ideal filter at frequencies near resonance. At resonance, the $\lambda/4$ stubs transform the shorts to opens, and current passes by as if the stubs were not there. Off resonance, the impedance is complex and poorly matched to the input ports, so it reflects power back. However, at an odd-integer multiple of the resonant frequency ω_o, there will be satellite bands where the stubs also transform the short to open. Additionally, at very low frequencies, the filter will look like a short to ground.

6.2.3 Differentially feeding a load-resistor

Finally, the microstrips terminate on 400 Å Ti sitting in close thermal contact with the TES (6.6). The incident radiation exceeds the band gap in Ti and this material is very lossy. However, for the antenna to operate in the D_{45^o} mode, the opposite transmission lines need a 180^o relative phase shift. We accomplish this by driving the 4-square piece of Titanium differentially, providing 20 Ω with a virtual ground at the center, properly terminating each 10Ω side.

The incident wave on the left of the load with voltage V_L partially reflects with with a voltage $(R-Z_o)/(R+Z_o)V_L$. The wave incident on the right will partially transmit a wave

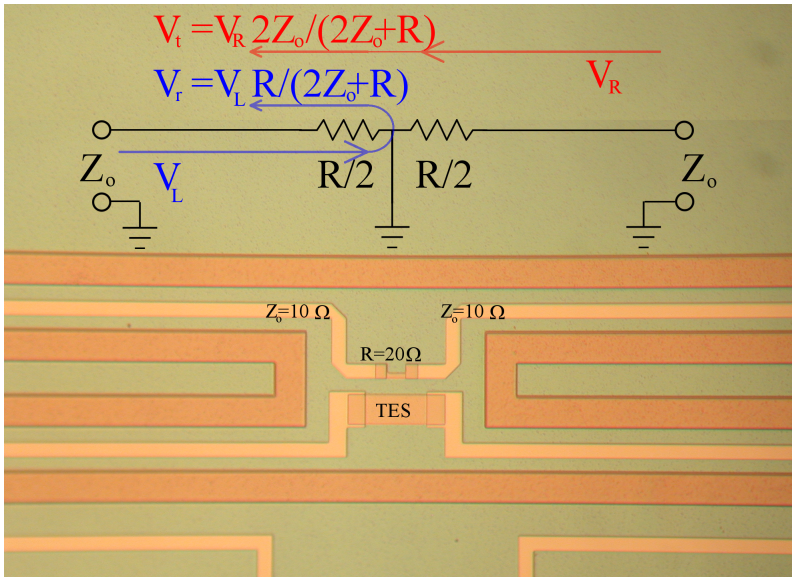

Figure 6.6. Picture of an un-released bolometer shows the Resistive load next to the TES. There is an equivalent circuit above and as well as voltage wave amplitudes. Blue is for waves originating on the left, red from the right.

with $(2Z_o)/(R+Z_o)V_R$ that interferes with the reflected wave. If the antenna only receives an odd antenna mode with V_L=$-V_R \equiv V_o$, then the voltage of the non-terminated wave

$$V = V_o \frac{R - 2Z_o}{R + 2Z_o} \tag{6.10}$$

which vanishes when R=$2Z_o$=20Ω. This design is fairly forgiving of errors in R; if R is 25% too low or high, it only reflects away 2% of the power. On the other hand, the antenna's unwanted even mode will have V_L=V_R, and this feed will reject 100 % of that power, regardless of the value of R.

To drive both polarizations, two of the transmission lines must cross in a microstrip cross-over (*Myers et al.* [2005]). This requires extra deposition and lithography steps that complicate the fabrication for what is intended as a simple test prototype. Instead, we only coupled one polarization to the bolometers, and terminated the other in lossy Al-Ti transmission line.

6.3 Optical Test Cryostat

We preformed all device measurements in an IR-labs dewar (serial number 576) retrofitted for optical measurements with a window and optical filter stack. Figure 6.7 shows a solid-works image of the dewar in cross-section as well as a photograph of the interior with radiation-shields removed.

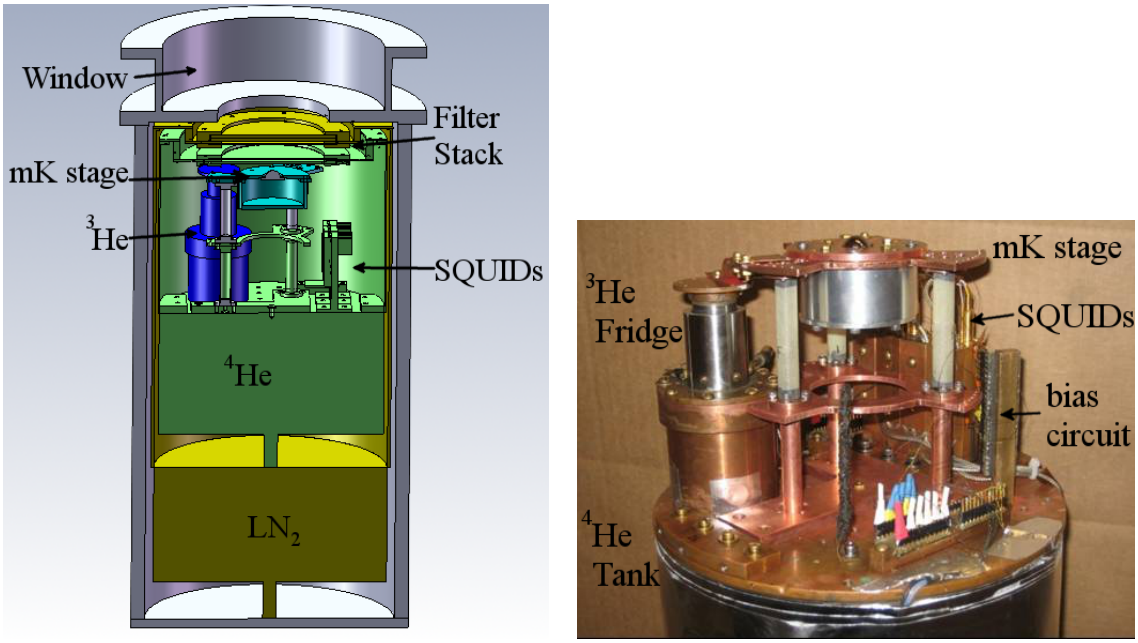

(a) Cross-sectional Dewar Drawing

(b) Photograph of Dewar interior

Figure 6.7. Stub filter with shorts through the square vias at the ends.

6.3.1 Dewar Cryogenics

The dewar buffers the millikelvin (mK) stage from room temperature (300K) with a Liquid Nitrogen (LN2) stage at 77K and a Liquid Helium (LHe) stage. While the helium boils at 4.2K at atmospheric pressures, we drop it's temperature to 1.3K by pumping. Each of these tanks enclose the inner stages with a radiation shield that we covered with 10-layers of Multi-Layer-Insulation (MLI) to insulate against radiative loading.

The mK-stage is cooled with a home-made closed-cycle ^{3}He sorption fridge. We drove helium from activated charcoal with heating resistor, allowing the helium to fall onto a 1.3K

condensation plate and collect on the fridge-head. Once we stop heating the charcoal, an annealed-tin heat switch thermally shorts it back to 1.3K, and the charcoal's large surface area pumps on the pool of ^{3}He, cooling it to temperatures as low as 0.26K (*Weisend* [1998]).

We isolated the mK-stage from the LHe stage on three 6.89mm (1.75") long Vespel legs with diameter 1.57mm(0.4") and wall thickness 0.020mm (0.005"). With a thermal conductivity of $k(T) = 1.8 \times 10^{-5} T^{1.2}$ W/m·K (*Woodcraft and Gray* [2009]), we estimate that the legs conduct roughly 6 nW, while the fridge is known to provide a cooling power of $\sim$10 nW. The cycle time for our ^{3}He fridge in these conditions varied between 6-12 hours.

6.3.2 Optical Filter Stack

We installed a 10.16cm (4") diameter 5.08cm (2") thick zote-foam window (*Takahashi* [2008]) on the bottom of the 300K shell. This foam has closed cells filled with N_2 gas, providing only modest scattering of millimeter radiation but sustaining vacuums of less than 1×10$^-$8 torr. It is crucial that the window hold such a low vacuum. We initially pump the dewar space with a turbo-pump, but after we transfer LHe, we remove the turbo and rely on cryo-pumping to keep the pressure low since the turbo vibrations provide unacceptable noise in our system.

We placed 0.762cm (0.3") of porous (expanded) Teflon at the LHe radiation shield window. Teflon absorbs Infra-red (IR) radiation, but it's index of refraction of 1.4 can reflect away some incident power. The company Porex creates porous Teflon by sintering Teflon particles in a way that leaves air voids, dropping the materials index of refraction. Measurements of the similar material Zitex suggest it's index is 1.2 (*Benford et al.* [2003]).

We also use a metal-mesh filter at 77K to reflect away radiation above 18 cm^{-1} wavenumber (540GHz). We installed additional low-pass metal mesh filters at the 4K radiation shield window that cut-off above 14 cm^{-1} (420GHz)and 12 cm^{-1} (360GHz). Peter Ade's group (University of Cardiff) provided these filters. There was ample room between the mK stage and the 4K window to optionally install an extra filter at 6 cm^{-1} (180GHz) to suppress the 90GHz filter's first satellite band as well as an optical attenuator to prevent saturation

from room-temperature thermal loads. Our attenuator was 0.635cm (0.25") of Emmerson-Cuming's MF110 pre-cast stycast material. It was not used with the devices of this chapter, but was used with those in the chapters 7 and 8.

6.4 Spectral Response

Our circuits operate in a 70-300 GHz spectral range where narrow-band coherent sources, such as those in network analyzers, are prohibitively expensive. Instead, we use a broadband thermal source and a Fourier Transform Spectrometer. The interferometer's source is a HPK 125W high-pressure mercury lamp from Msscientific (previously manufactured by Philips) that sits at the focus of a collimating parabolic mirror. Our interferometer is shown in Figure 6.8. A nominally 0.039mm (0.010") thick sheet of mylar splits the beam between two arms, one with a fixed mirror (top) and a second one with a movable mirror (right). The beams re-combine in the mylar and are redirected into the dewar with light-pipe.

The end of the light-pipe acts as a isotropic point source and we re-converge the beam onto our devices with a warm (300K) TPX-lens. The TPX lens focal-ratio was roughly f/2.5, while the detector's ratio varies from f/5.7 at the upper band edge to f/2.2 at the lower edge. As a result, the radiation from the interferometer over-illuminates the antenna's fundamental mode at all but the lowest frequency channel and the antenna receives only $A\Omega = \lambda^2$ throughput over most of the band. This simplifies the analysis because a lens that under-illuminates the antenna would produce measured spectra that are a convolution of the filter and throughput spectra.

If the bulb were a monochromatic source that emitted only a wavenumber $\bar{\nu}$ with intensity I_o, then when the mirrors have a path-length difference $\Delta = 2(d_1 - d_2)$, the device under test will receive an intensity

$$I(\Delta) = I_o/2\left[1 + \cos\left(2\pi\bar{\nu}\Delta\right)\right] \tag{6.11}$$

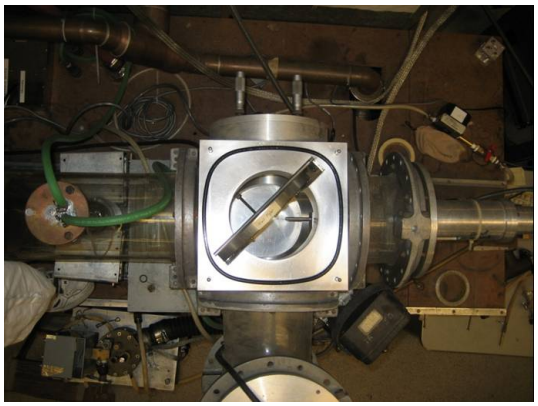

(a) Fourier Transform Spectrometer (FTS)

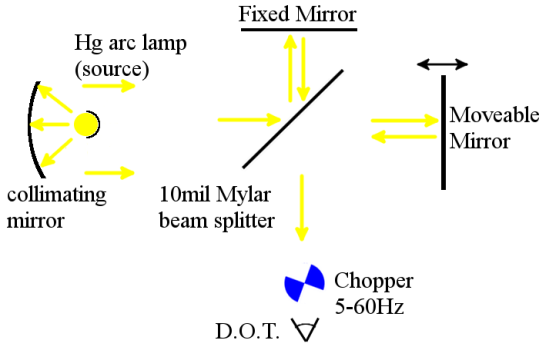

(b) FTS Schematic

Figure 6.8. (a) Photograph of FTS Spectrometer used in these measurements, viewed from above. The dewar with the Device Under Test (DUT) is not visible. (b) Schematic of FTS optics.

However, the bulb actually emits a broad spectrum and the bolometer will see a wide fractional bandwidth with a spectrum $I(\bar{\nu})$ that is defined by both the Device Under Test (DUT) *and* the interferometer's optics. Integrating Equation 6.11 over $\bar{\nu}$ with intensity $I_o = I(\bar{\nu})d\bar{\nu}$ yields the total power the bolometer receives at each mirror position Δ:

$$J(\Delta) = I_o/2 + \int_{\bar{\nu}=0}^{\infty} \frac{I(\bar{\nu})}{2} \cos\left(2\pi\bar{\nu}\Delta\right) d\bar{\nu} \tag{6.12}$$

In principle, we can recover the system's spectral response $I(\bar{\nu})$ from the Fourier Transform of the interferogram $J(\Delta)$. In practice, we only sample the interferogram at finite steps

over a finite total length and perform a discrete fast-fourier-transform on the data. The step spacing between mirror positions determines the maximum resolvable frequency, so we must sample the interferogram at sufficiently fine steps to Nyquist sample the spectrum up to the lowest optical-filter cutoff at 12 cm^{-1} (360GHz). The throw of the movable mirror arm is 42mm, which limits the spectral resolution of $I(\bar{nu})$ to 0.06 cm^{-1} (1.8GHz) (*Bell* [1972]).

The measured spectra are the product of those from the interferometer, dewar, and DUT. However, we are primarily interested in the response of only the detector, so we normalized the spectrometer against a different bolometer within a different dewar with a known and constant spectral response. Dividing the DUTs' spectra by the normalization spectrum removes the "null" in the beam-splitter at 330GHz and other spectral properties of the spectrometer optics.

Finally, we normalized the spectra's total optical throughput by measuring the power received from a chopped 77-300K thermal source (with δT=223K) that fills the antenna beam. The single-moded antenna can receive at most

$$\Delta P = k\Delta T \int I(\bar{\nu}) d\nu \tag{6.13}$$

while the a bolometer operated in strong electrothermal feedback will receive

$$\Delta P = V_b \Delta I_{SQ} \tag{6.14}$$

as discussed in chapter 3. The ratio of the two powers ΔP is the total camera fractional throughput (including optical filters).

Figure 6.9 shows the normalized spectral response of four devices centered at different frequencies. We fabricated an additional one that would have received power centered at 150GHz as well as a device with no filters, but design errors compromised those devices. The bold percentages show the band-averaged optical throughput through our test dewar to the bolometers. The inefficiencies are closely mirrored by simulations that account for

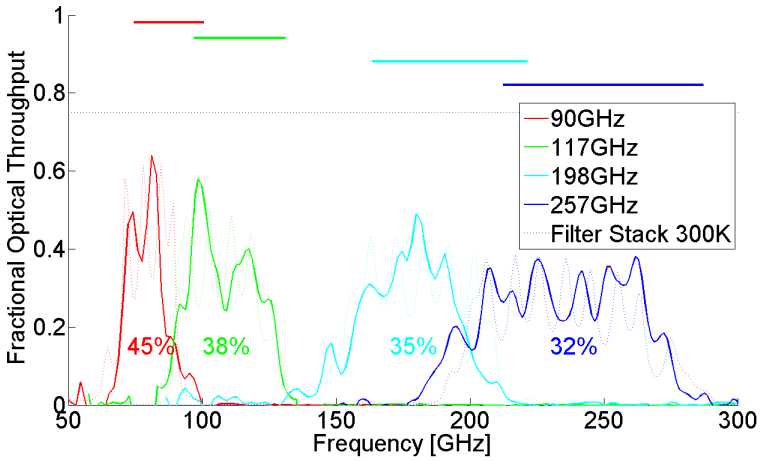

Figure 6.9. Solid curves show measured spectra, the colored dashed lines show simulations of the filter with microstrip lines between antenna and bolometer load. The dashed line is the average transmission of the filter stack at 300K. The solid lines at the top depict the designed -3dB bandwidths.

loss in the optical filter stack, reflections at the antenna-microstrip, and microstrip-load interface, reflections at the contacting lens surface, and dielectric loss in the microstrip.

The downward slope of throughput as frequency increases is due to the lossy transmission lines having a longer electrical length at those frequencies and suggests a loss-tangent of $\tan(\delta) = 0.008 \pm 0.002$, which is consistent with our group's previous measurements of loss-tangent in our SiO_2 of $\tan(\delta) = 0.005 \pm 0.001$. We summarize the other sources of loss in Table 6.1 and note that the expected fractional throughput is similar to the measured values. However, the throughput through the filter stack is poorly understood because we have only performed the measurements warm in the middle of a gap in light-pipe.

Table 6.1. Losses in the single filter sinuous devices

Component	Power Transmitted
Optical Filters	≈70%
curved AR-coating	86%
Antenna Front-lobe	91%
Antenna-microstrip interface	88%
Dielectric Loss	70-90%
Total	35-45%

The solid bars at the top of the spectrum depict the filters' designed bands (-3dB).

The spectral band centers are all 9% lower in frequency than designed, which is likely caused by wavespeeds $(LC)^{-1/2}$in the lines being 10% lower than expected, or LC being 23% higher. We control the SiO_2 dielectric thickness to a high level of precision (around 5%). In Section 8.6, we compare pass-bands of this type with a different design to conclude that the oxide permittivity is likely $\epsilon_r = 0.46$ and that the Niobium's surface inductance is $L_s = 0.18$ pH/sq. Our group is currently developing techniques to test our lithographed circuit components at 4K, but at slightly lower frequencies of 40GHz and we hope to resolve this issue in the near future.

We designed our filters to have a -3dB fractional band-width of 30%. With the exception of the 90GHz channel, all the bands have a best fit width that is within an error-bar of design. The 90GHz channel fits to a narrow 22% fractional width because the upper-third of the band's transmission is supressed. We do not understand what causes this, but it is present in the 90GHz channels in later chapters. Again, we hope our scale-model measurements may shed light on this.

We also observe significant fringing within the bands, which we attribute to a fabry-perot cavity between impedance mismatches somewhere within our optics or microwave circuits. If the impedance mismatches produce voltage reflection coefficients $R_1(\nu)$ and R_2 and transmission coefficients $T_1(\nu)$ and T_2 at each of the two interfaces and there is a phase delay $\Delta\phi(\nu)$ for each pass, then the total transmission from all partial waves is:

$$|T|^2 = TT^* = \frac{|T_1(\nu)T_2|^2}{1 - 2\,|R_1(\nu)R_2|\cos(2\Delta\phi(\nu)) + |R_1(\nu)R_2|^2} \tag{6.15}$$

(*Born and Wolf* [1999]). We can identify the source of fringing by comparing the fringe-spacing in spectra with the phase-differences ($\Delta\phi(\nu)$) between different possible mismatches and we can then constrain the product of reflection coefficients $R_1(\nu)R_2$ (and hence impedances) through the fringe depths. As discussed in Chapter 5, the antenna impedance should be on average 105Ω with reactance that is at most $\pm$20Ω (which is why $R_1(\nu)$ and $T_1(\nu)$ bear a frequency dependence on Equation 6.15). Further we measured the bolometer loads with a resistance bridge to be 26 Ω (13 Ω between the microstrip line and virtual

ground). The phase shift a wave experiences between two mismatches reflects the changing wave speed on the impedance transformer in the antenna feed as well as the greatly reduced wave speed in the filter and produces an average fringe-spacing of 8.2GHz, which closely matches the fringe spacing in our spectra of 8.7 ± 0.4 GHz (averaged over the all bands). The dashed lines in Figure 6.9 include not only the filters, but also the simulated antenna impedance, measured load resistance, lines in between, and loss in the optical filter stack. The ratio of fringed trough to peak averaged across all bands is 0.63 ± 0.12, while the simulations suggest an average value of 0.57. This agreement suggests that our measurements are consistent with an antenna impedance simulated and modeled in chapter 5. However, Figure 6.9 reveals only a rough similarity between simulation and experiment through a few statistical parameters; the simulations clearly show differences from the measurements suggesting systematic effects that our simple model does not reflect.

Lastly, it is possible that the bolometer itself is inefficient in transferring the thermal power from the load to TES. However, our group has previously characterized similar bolometers' transfer functions by driving the RF-termination with a DC power supply (instead of an antenna). We found that the power received in the TES matches that deposited from the DC supply (*Myers* [2008]).

6.5 Beam Patterns

The spatial distribution of power reived by the bolometers is just as important as the frequency distribution when characterizing our device. However, our bolometers will average over all frequencies transmitted through the in-band filter, so it is most useful to measure the beam-patterns with a broadband source. Figure 6.10 shows the setup for these measurements. Our source is a 300-77K chopped thermal load with an aperture size of 1.27cm (0.5") that sits in a plane (5" to 11.5") below the plane with the contacting lens' tip. We moved the source within a plane on the pair of linear translation stages seen in Figure 6.10.

The un-polarized beam maps are shown in Figure 6.11: Figure (a) shows 2-D simulations, (b) 2-D measurements, and (c) simulations (dashed lines) and measurements in three

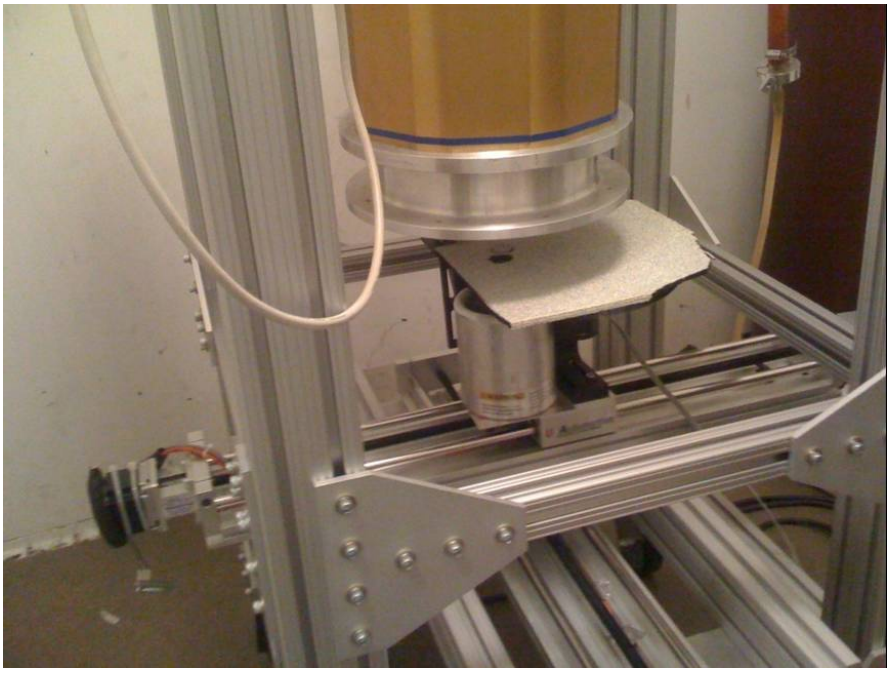

Figure 6.10. Chopped thermal load used for pattern measurements. We extended the 300K surface defining the aperture with more eccosorb than shown to completely block the chopping wheel everywhere except the aperture.

cuts through the beam. As the source moves off axis by an angle of θ, the area subtended by the source decreases by $\cos(\theta)$, so we have corrected the powers in these maps by that factor. Additionally, the simulated beams in (a) are an average of patterns weighted by the measured spectral response seen in Figure 6.9, all normalized to their peak power on boresight.

Figure 6.11.c shows that the measurements seem to agree more closely with simulation in the higher two frequency channels than at the low ones, but none agree well enough to have a low reduced χ^2. The simulations account for the presence of the lens with a single-layer anti-reflection coating, but they do not account for the rays (10% of power) that partially reflect between the antenna and lens surface. Nor do they account for reflections off the low-pass metal-mesh filters that are notorious for complicating beam patterns in cameras. These systematics may explain some of the observed discrepancies.

The best fit beam widths are shown in Table 6.2. As the center band frequency increases from 83GHz to 230GHz (a factor of 2.8), the beam only narrows by 2.5. This discrepancy

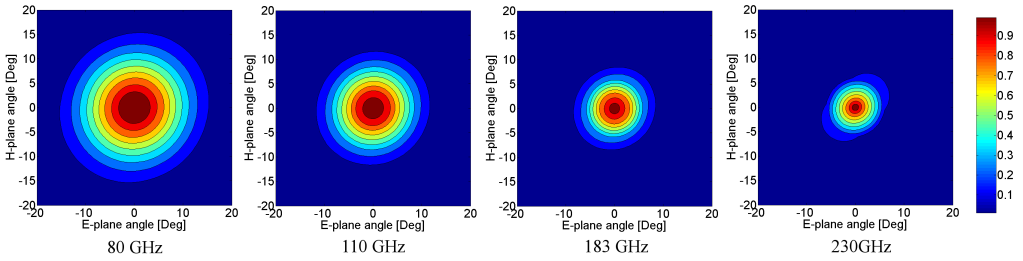

(a) 2-D Beam Simulations

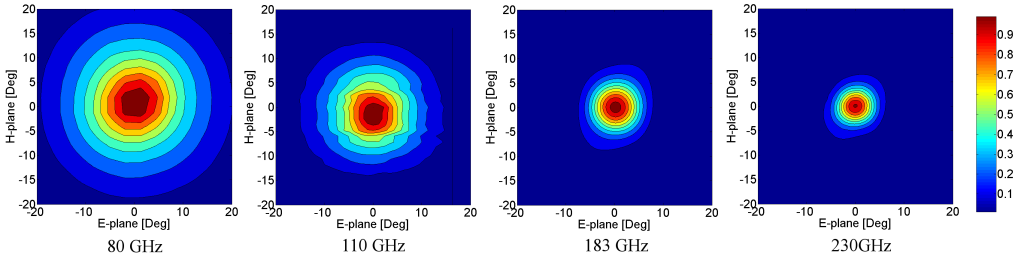

(b) 2-D Beam Measurements

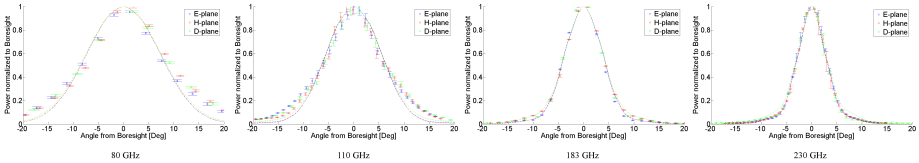

(c) Beam Cut Simulations and Measurements

Figure 6.11. Simulations and Measurements of Sinuous Beams

arises because the lens is not a true synthesized ellipse, but is rather between the elliptical and hyperhemispherical geometries, which suppresses the decrease in beam size.

6.6 Cross-polarization Rejection

As stressed in Chapter 5, this antenna must efficiently reject cross-polarized power if it is to be useful for polarimetry. If an antenna is well aligned to a polarized source, it should reject all cross-polarized power on boresight over a narrow band. The polarization tilt wobble ensures that the band-averaging bolometers will see a small amount of the wrong polarization.

Table 6.2. Beam Geometry

Channel	ellipticity	E-plane FWHM	H-plane FWHM	Boresight Cross-Pol Rejection
80 GHz	$1.1\% \pm 0.2\%$	$15.1^o \pm 0.7^o$	$15.6^0 \pm 0.7^o$	
110 GHz B	$2.8\% \pm 0.2\%$	$10.9^o \pm 0.4^o$	$11.8^o \pm 0.4^o$	
183 GHz B	$0.4\% \pm 0.1\%$	$8.1^o \pm 0.3^o$	$8.2^o \pm 0.3^o$	
230 GHz B	$2.0\% \pm 0.2\%$	$5.9^o \pm 0.3^o$	$6.2^o \pm 0.3^o$	

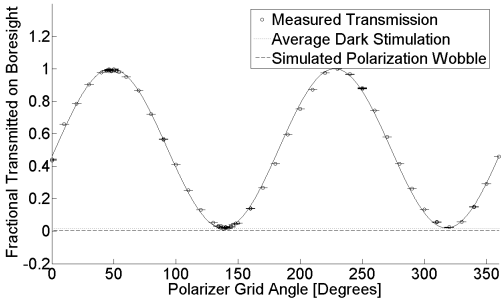

Figure 6.12. Power transmitted from a chopped thermal load on boresight to antenna through a polarizing grid. This antenna's circuit filtered the 110GHz band; other devices with different filters had similar polarization response.

We characterized this leakage by placing the chopped thermal load from Figure 6.10 on boresight and rotating a polarizing grid between the load and dewar window. Figure 6.12 shows the result of this measurement and best fit line for one of the channels and has the expected sinusoidal form. Table 6.2 summarizes the fraction of cross-polarized power leaked from all the channels, and it is roughly 2% on average. The grid itself is known to leak between 1-2% (*Myers* [2008]), which explains most of the systematic offset between the grid and the expected leakage from wobble.

6.7 Conclusions

In this chapter, we have demonstrated that TES bolometers can be coupled to the sinuous antenna in a way that is very similar to the Polarbear feeding scheme. This design provides high optical coupling efficiency with desirable beam characteristics. However, the differential feeding scheme requires complicated wiring or broadband hybrids if it couples

to bolometers through the channelizer circuits in Chapters 7 and 8. Since these alternatives are difficult to implement, we did not use the slot-coupling in the later designs.